Electronic Supplementary Material (ESI) for Journal of Materials Chemistry A.

Depth-dependent oxygen redox activity in lithium-rich layered oxide cathodes

Andrew J. Naylor[a]†, Eszter Makkos[b], Julia Maibach[c], Niccoló Guerrini[a], Adam Sobkowiak[a], Erik Björklund[c], Juan G. Lozano[a], Ashok S. Menon[c], Reza Younesi[c], Matthew R. Roberts[a], Kristina Edström[c], M. Saiful Islam[b], Peter G. Bruce[a,d,e]

[a] Department of Materials, University of Oxford, Parks Road, Oxford OX1 3PH, United Kingdom

[b] Department of Chemistry, University of Bath, Bath, BA2 7AY, United Kingdom

[c] Department of Chemistry – Ångström Laboratory, Uppsala University, Box 538, SE-75121 Uppsala, Sweden

[d] The Henry Royce Institute, Parks Road, Oxford, OX1 3PH, United Kingdom

[e] The Faraday Institution, Quad One, Becquerel Avenue, Harwell Campus, Didcot, OX11 0RA, United Kingdom

† Current address: Department of Chemistry – Ångström Laboratory, Uppsala University, Box 538, SE-75121 Uppsala, Sweden

Supplementary Information

Note 1. Depth of analysis calculations.

For energy-tuned photoelectron spectroscopy measurements, three different photon energies (1.09, 2.35, 7.05 keV) were used to probe different depths of the sample. The inelastic mean free path (IMFP) of an electron is highly dependent on its kinetic energy. Those photoelectrons emitted as a result of excitation by a higher photon energy (e.g. 7.05 keV) will have higher kinetic energies and will therefore have a greater probability of travelling a longer distance before being inelastically scattered. In contrast, electrons with lower kinetic energies are more likely to have been emitted from close to the surface. The majority (~95 %) of electrons are emitted from a depth corresponding to 3x IMFP.[1] While we employ a grazing incident angle to capture an average signal of many particles on the sample and minimise radiation damage, the analyser is oriented 90 ° to the sample to ensure the highest possible probing depth.

Whilst the IMFP varies greatly with electron kinetic energy, it is also somewhat dependent on the nature of the solid from which the electrons are emitted, taking into account factors such as density, band gap, molecular weight, and number of valence electrons. For the layered transition metal oxide cathode material that we investigate in this study, we used the following parameters in the calculation of analysis depth:

Electron kinetic energy, E_K (O 1s): [hν = 1.09 keV] 560 eV

[hν = 2.35 keV] 1820 eV

[hν = 7.05 keV] 6520 eV

Number of valence electrons in pristine material, N_V: 16.6

Density, ρ: 4.19 g cm^{-3}

Molecular weight, M_W: 85.0306 g mol^{-1}

Band gap energy E_g: 2.5 eV – as calculated from density of states (DOS) for the $Li_{1.17-x}Ni_{0.25}Mn_{0.58}O_2$ structure.

Approximating the IMFP using these parameters and the equations of Tanuma, Powell, and Penn (TPP-2M)[2], we estimate that 3x IMFP corresponds to a depth of 4.12 nm for a photon energy of 1.09 keV, 10.06 nm for 2.35 keV, and 28.69 nm for 7.05 keV. We note that, as with any formula, the TPP-2M experiences limitations and assumptions, so these values should only be taken as approximations. This is represented in the schematic diagram in Figure 1 of the main text where monochromatic light of three different energies is signified to be ejecting photoelectrons from different depths of a particle. In practice, not just one particle is being probed, but an average signal is acquired from a large number of particles. This serves as an approximation for the depth of analysis for each photon energy used and when probing the O 1s core level. For partially, or fully charged states the properties (e.g. band gap) of the material will change. However, as previously mentioned it is the kinetic energy that most affects the IMFP.

While the majority (95 %) of electrons are ejected from a depth corresponding to 3x IMFP, the probability of escape decreases exponentially, as shown in Figure S1. This is inherent of photoelectron spectroscopy measurements, resulting in that they are surface-sensitive. However, by using large enough probing depths a part of the signal will originate additionally from the bulk of the material.

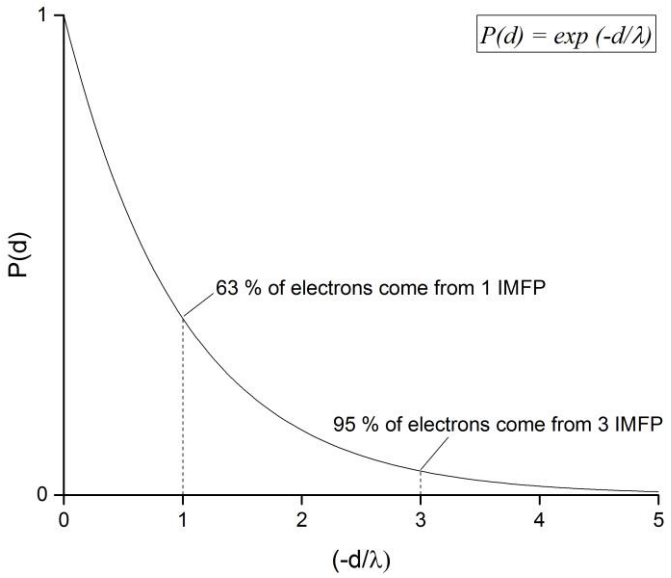

Figure S1. The probability of escape of an electron from a given depth, *d*, where λ is the inelastic mean free path for electrons of energy E.[3]

A simple calculation involves assuming that, rather than a concentration gradient being formed by a newly detected species through an existing structure, a well-defined surface layer forms on top of the material. If a 1 nm surface layer forms on top of the particle, then the % of electrons originating from that layer for each excitation energy used in this study is as follows:

	1.09 keV	**2.35 keV**	**7.05 keV**
1x IMFP (λ)	1.37 nm	3.35 nm	9.56 nm
d/λ	0.73	0.22	0.02
% e^- from surf. layer	51.8 %	25.8 %	9.9 %

i.e. for 1.09 keV, we integrate between 0 and (1 nm/1.37 nm): [exp(0)-exp(-0.73)]

The remainder of the signal from each measurement comes from the bulk 'layer', deeper than the 1 nm surface layer. By calculating and plotting theoretical relative intensities (Figure S2) for such a layered system, it is possible to see how the relative intensity for the surface layer rapidly decreases when using large excitation energies corresponding to high probing depths.

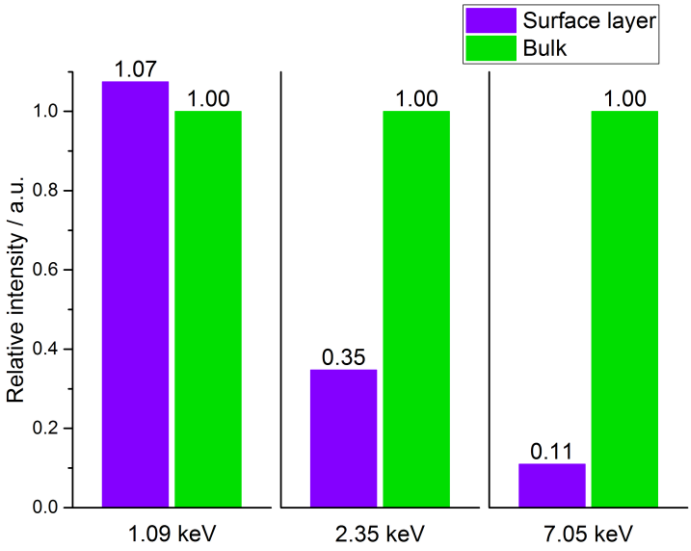

Figure S2. Theoretical relative intensities for a 1 nm surface layer on a bulk material for three different excitation energies (corresponding to three different probing depths). Intensities are normalised to the bulk layer signal.

This effect is even more pronounced for a thicker surface layer (5 nm) with 97.4 % of the signal coming from the surface layer at 1.09 keV excitation energy and 40.7 % from the surface layer at 7.05 keV. This situation demonstrates how spectra would appear if a well-defined surface layer existed rather than an intermixing of species from the surface to the bulk, forming a concentration gradient. In the other extreme case where a sample has a completely uniform distribution of two species from surface to bulk, the spectra would appear independent of excitation energy.

Note 2. Fitting of the O 1s spectra.

A concise method for fitting of the O 1s spectra was employed, while using the minimum number of peaks necessary in the fitting model and justifying, in chemical terms, certain features of the model.

1. From the surface analysis of the $Li_{1.2}Ni_{0.2}Mn_{0.6}O_2$ pristine sample, using a photon energy of 1.09 keV, the binding energy (BE) positions for surface-bound species were determined and propagated across the spectra for all samples at all photon energies. Only a shift of ±0.15 eV (to allow for instrumental limitations) was permitted for each peak, since there is not expected to be any surface layer deposition during charge. This is verified in the C 1s spectra (Figure S4) where very little intensity for surface species, such as carbonyls or carbonates, is observed on any of the charged electrodes. We additionally verify that there is no reaction between the pristine electrode and the electrolyte (see below for details). While some surface deposition is suspected in the discharged sample, likely due to decomposition of the electrolyte, the peaks are fitted with the same constraints as there is no noticeable change in their positions. Additionally, the O 1s spectra for the spinel-phase LMNO electrodes show no change in binding energy for the surface-bound species during charge. In the spinel material, no other species are expected other than the O^{2-} and surface-bound species since it does not exhibit oxygen redox activity.
2. With the constraints in place for the surface-bound species, the intense peak for O^{2-} is allowed to fit without constraints at ~529 eV. In the pristine sample, this results in a very acceptable fit, as expected, where the fitted model overlays closely with the raw data set. However, for the charged samples another peak corresponding to oxidised oxygen (O^{n-}) must be included in the model in order for the fit to align almost exactly with the raw data. From the sample charged to 4.8 V, a splitting of 1.2 eV ± 0.15 eV was determined to result in the best quality fit. This rule was propagated across all spectra, the position for the O^{n-} peak determined by subtracting 1.2 eV from the O^{2-} peak, allowing to fit, and repeating iteratively.

The positions for these peaks are therefore not fixed across samples (described in the main text) and move relative to the surface-bound species (these can be treated as separate layers with distinct chemistries and reactivities); however, the constant splitting represents that the two transition metal oxide peaks are within similar crystal structure environments and differ mainly in their oxidation states.

3. The full width at half maximum (FWHM) of the O^{2-} peak has a maximum of 1.2 eV, while that of the O^{n-} peak exhibits a slightly higher value of 1.6 eV, due to potentially greater disorder in the oxidised state. The surface-bound species have FWHM maxima of 2.1 eV for the lower BE peak and 2.5 eV for the higher BE peak. The broadness of these peaks can be attributed to these peaks likely representing multiple surface components of slightly different binding energies. Such ranges are defined to allow for expected variation between samples or from surface to bulk within a sample. The FWHM can vary with crystallinity, disorder, oxidation state, chemical bonding, and instrumental effects among others and these factors are particularly influential when comparing the surface and bulk of a material.
4. Some satellite peaks are visible for a few charged samples at higher binding energy (535 – 536 eV) to the peaks of interest. It is not known from where these originate, but does not appear to be a result of charging since we would otherwise likely observe such behaviour in other core level spectra and to a greater extent in other samples.
5. O 1s spectra for the spinel-phase LMNO and the multiple cycles $Li_{1.2}Ni_{0.2}Mn_{0.6}O_2$ were fitted by a similar method.

Peak fitting parameters have been determined by referring to previous studies.[4–9]

The fitting specification is shown in the table below.

Table S1. Fitting specification of O 1s spectra for $Li_{1.2}Ni_{0.2}Mn_{0.6}O_2$ and $LiNi_{0.5}Mn_{1.5}O_4$. BE: Binding Energy; FWHM: Full Width Half Maximum; $Surf_1$ + $Surf_2$: Surface-bound species; Sat.: Satellite peak.

$Li_{1.2}Ni_{0.2}Mn_{0.6}O_2$		O^{2-}			O^{n-}		
	Excitation Energy / keV	**BE / eV**	**FWHM / eV**	**% area**	**BE / eV**	**FWHM / eV**	**% area**
Pristine	1.09	529.2552	1.1289	60.73	-	-	-
	2.35	529.0574	1.0530	68.18	-	-	-
	7.05	528.9276	1.0336	83.71	-	-	-
4.1 V	1.09	528.9210	1.1371	45.33	530.2699	1.6	17.59
	2.35	528.8467	1.0062	64.29	530.1896	1.5893	17.38
	7.05	528.8060	0.9686	83.87	530.1599	1.5927	9.27
4.55 V	1.09	528.8821	1.1305	36.04	530.2373	1.5994	34.68
	2.35	528.6921	1.0541	48.06	529.9521	1.5998	34.61
	7.05	528.5916	1.0374	61.15	529.8520	1.5157	25.69
4.65 V	1.09	528.8309	1.1466	40.50	530.1197	1.5997	37.26
	2.35	528.7067	1.0933	50.69	529.9066	1.5995	38.76
	7.05	528.5611	1.1449	58.83	529.6791	1.5790	29.09
4.8 V	1.09	528.8655	1.2000	34.62	530.1576	1.6000	26.29
	2.35	528.7539	1.1011	50.34	529.9746	1.6000	34.01
	7.05	528.6938	1.1925	64.73	529.8669	1.5713	24.07
Discharge (2 V)	1.09	529.4639	1.0712	33.27	530.8172	0.6096	0.67
	2.35	529.3144	1.0816	54.74	530.6114	1.3800	3.16
	7.05	529.2384	1.1534	77.34	530.5881	0.9121	4.10
10 Cycles (2 V)	1.09	529.6208	1.0283	44.77	530.6734	0.9408	1.29
	2.35	529.4572	1.0536	61.98	530.5572	1.2740	4.74
	7.05	529.3487	1.1295	76.99	530.6428	1.1834	9.42
10.5 Cycles (4.8 V)	1.09	529.0805	1.1707	42.23	530.4407	1.2169	12.46
	2.35	528.8322	1.1899	59.67	530.0401	1.5982	15.97
	7.05	528.6010	1.2000	61.52	529.6521	1.5999	22.56
$LiNi_{0.5}Mn_{1.5}O_4$							
Pristine	1.09	529.4113	0.9554	60.03	-	-	-
	2.35	529.2876	0.9367	75.41	-	-	-
	7.05	529.2431	0.9812	82.68	-	-	-
4.75 V	1.09	528.9906	1.0887	37.15	-	-	-
	2.35	528.7859	0.9746	57.49	-	-	-
	7.05	528.6999	1.0149	75.06	-	-	-
5V	1.09	529.0019	1.092	33.3	-	-	-
	2.35	528.7874	0.9813	51.01	-	-	-
	7.05	528.6986	1.0098	67.33	-	-	-

Surf$_1$			Surf$_2$			Sat.			
BE / eV	FWHM / eV	% area	BE / eV	FWHM / eV	% area	BE / eV	FWHM / eV	% area	Residual STD
531.3713	1.7748	30.40	532.5773	2.2535	8.87	-	-	-	8.54
531.3349	2.0990	24.17	532.6993	2.5000	7.65	-	-	-	10.39
531.3791	2.1000	11.99	532.5959	2.2505	4.30	-	-	-	2.95
531.2501	1.8296	29.71	532.7906	2.0836	7.37	-	-	-	11.58
531.1705	1.5337	13.89	532.8242	2.0266	4.44	-	-	-	16.43
531.2501	1.454	5.82	532.85	1.4301	1.04	-	-	-	3.95
531.2503	1.7930	14.96	532.7022	2.3759	9.59	536.8181	2.7502	4.74	6.05
531.2502	1.7802	10.43	532.7654	2.0071	5.65	535.0034	2.0438	1.26	7.41
531.3037	1.9783	5.00	532.8331	2.2421	5.21	535.1168	2.2162	2.96	3.25
531.2503	1.9875	15.86	532.8215	1.9958	6.38	-	-	-	6.83
531.3521	1.7613	5.90	532.8500	2.4994	4.66	-	-	-	7.05
531.3869	1.5048	3.45	532.8025	2.1850	3.52	534.7836	1.6713	5.10	2.82
531.2500	2.0995	25.48	532.5864	2.1216	13.61	-	-	-	6.87
531.3351	2.0346	10.28	532.6995	2.0366	4.47	534.8185	1.3345	0.90	6.96
531.4713	1.6469	5.70	532.5500	1.2662	1.91	534.6233	2.3175	3.59	2.44
531.3274	1.6214	43.74	532.5500	2.4202	22.32	-	-	-	6.63
531.2502	1.6896	28.87	532.7393	2.4967	13.23	-	-	-	10.30
531.2502	1.3608	11.50	532.6011	2.2735	7.06	-	-	-	4.03
531.4168	1.4766	31.50	532.8498	2.3404	22.44	-	-	-	5.29
531.2626	1.5822	18.80	532.8471	2.3810	14.47	-	-	-	8.25
531.4365	1.3137	6.53	532.7277	2.2185	7.07	-	-	-	4.16
531.2500	1.7189	20.07	532.7580	2.1344	25.24	-	-	-	3.98
531.2508	2.0025	11.18	532.7017	2.4991	13.19	-	-	-	5.07
531.3420	1.4476	6.15	532.5856	1.3989	3.06	534.4071	2.2162	6.70	2.59
530.8816	2.2	31.76	533.0147	2.5168	8.21	-	-	-	2.88
530.6257	2.1993	17.39	532.5006	2.9619	7.2	-	-	-	5.13
530.4821	2.1984	10.83	532.6908	2.967	6.49	-	-	-	2.55
530.7887	1.8227	38.08	532.6164	2.1807	24.77	-	-	-	3.02
530.4892	2.0822	28.73	532.5453	2.1773	13.78	-	-	-	5.03
530.3001	2.1962	17.56	532.6816	2.2624	7.38	-	-	-	3.29
530.8734	2.0054	39.63	532.7892	2.0718	27.07	-	-	-	2.83
530.5813	2.2	28.98	532.6341	2.2358	20	-	-	-	4.99
530.3017	2.1999	17.6	532.8165	2.9626	15.06	-	-	-	3.18

In order to verify that there is no reaction between the pristine electrode and the electrolyte, a soaking experiment was conducted for several hours. A comparison of the O 1s spectra for the pristine electrode, the unwashed electrode and the washed electrode after soaking is shown in Figure S3.

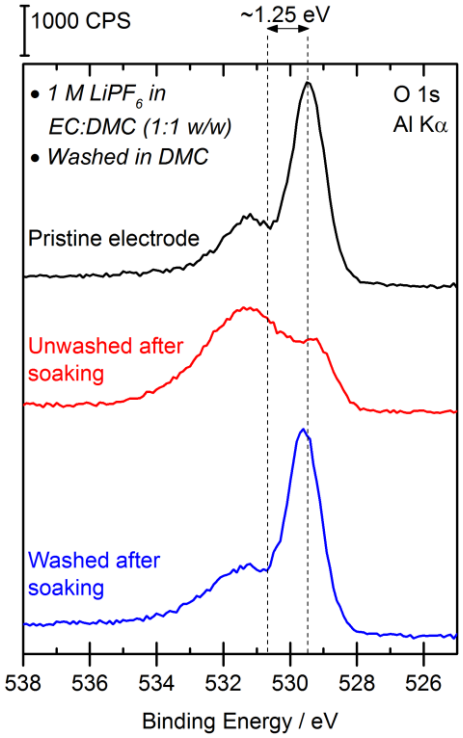

Figure S3. O 1s spectra of the pristine $Li_{1.2}Ni_{0.2}Mn_{0.6}O_2$ electrode compared with that soaked in electrolyte for several hours, then either washed in DMC or not washed, and allowed to dry in an argon atmosphere. The measurements were performed on an in-house XPS using an Al Kα source.

Note 3. C 1s spectra for $Li_{1.2}Ni_{0.2}Mn_{0.6}O_2$ samples.

Photoelectron spectra were energy calibrated to the carbon black peak at 284 eV in the C 1s spectra, as presented in Figure S4.

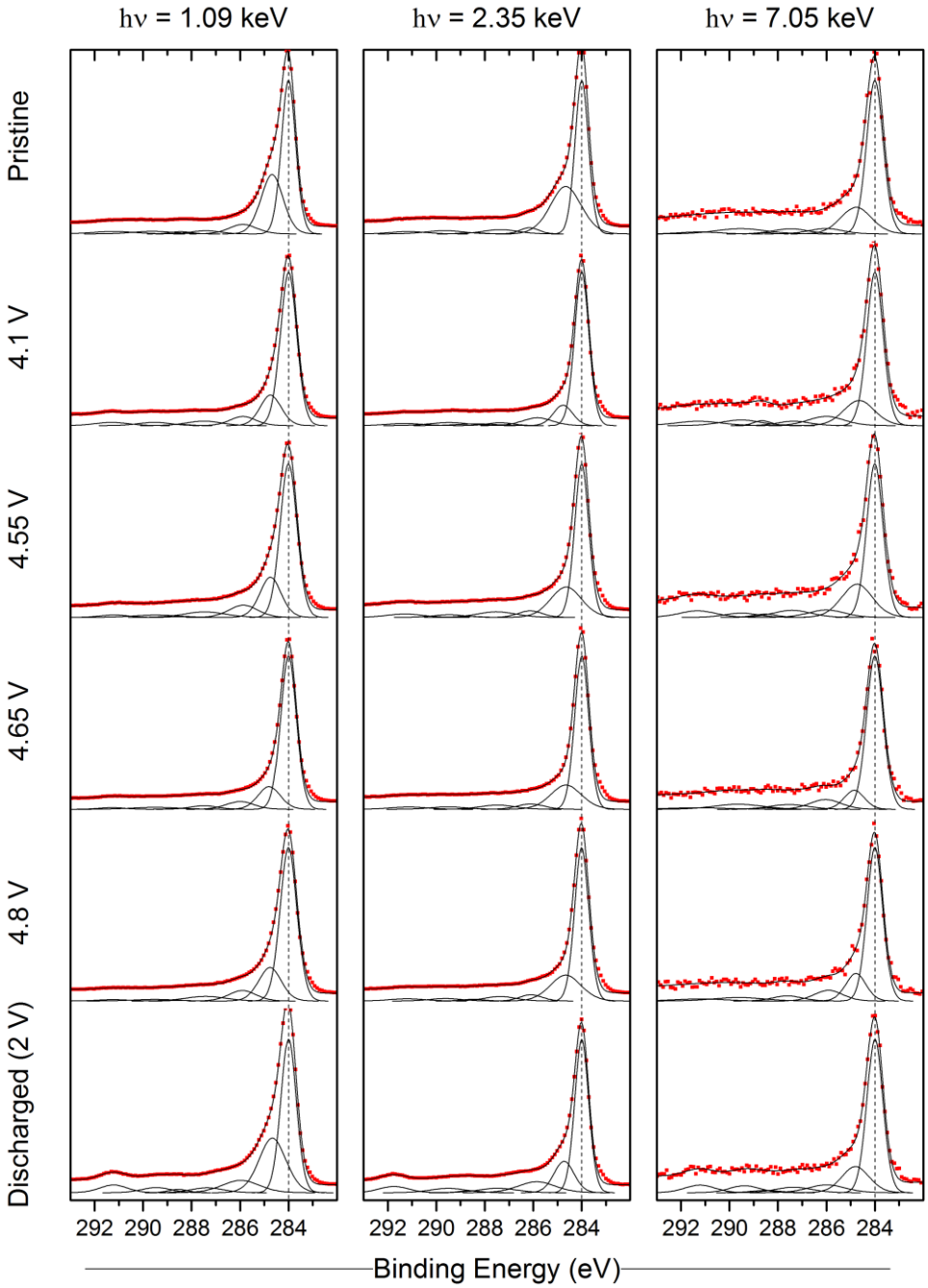

Figure S4. C 1s spectra for $Li_{1.2}Ni_{0.2}Mn_{0.6}O_2$ samples, measured at three different photon energies. The vertical lines indicate the position of the carbon black C=C peaks at 284 eV, used to energy calibrate all other spectra.

Note 4. Energy scale linearity check with sputter cleaned silver single crystal.

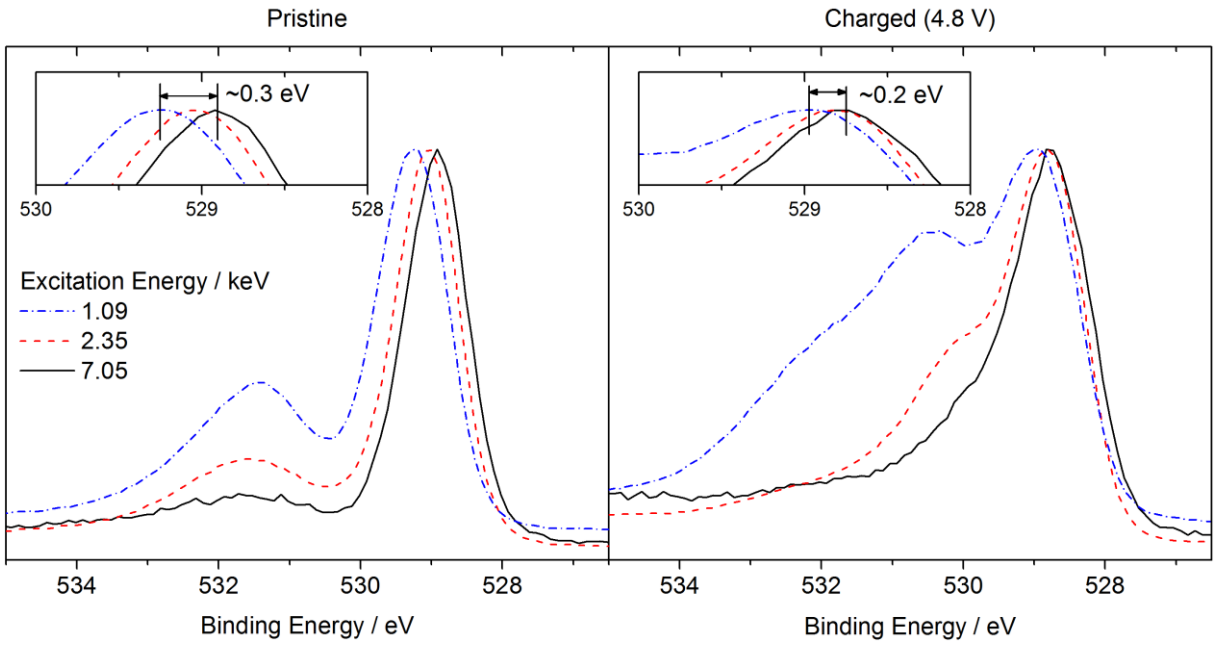

Figure S5. O 1s spectra for pristine and charged (4.8 V) materials, indicating the small excitation energy dependent shift.

The small excitation energy dependent shift we observe in the O1s spectra (Figure S5) has been resolved after energy calibration to the carbon black (C=C, 284 eV) in the C 1s spectra, which has a high intensity in all samples. When understanding the origin of this shift, we can disregard charging of the samples since they have a reasonable quantity of electronically conductive additive within the electrode, and are well connected to the sample plate. In addition, observations consistent with charging would typically be characterised by distortion of other core level spectra (not just the O 1s spectrum), broadening of peaks, and peak shifting of several eV.

In order to check the instrument for energy shifting (non-linearity) aside from that caused by chemical effects, the surface of a Ag(111) single crystal was prepared *in situ* via three cycles of sputtering (Ar^+ ions, voltage 1 keV, emission current 10 mA, duration 20 mins) and annealing (temperature ~550 °C, duration 20 mins). Silver was chosen because it has two transitions (Ag 3d and Ag 3p) within the binding energy range of interest in the current study, which would highlight any

non-linearity due to the moderate energy difference between them. These sputtering-annealing cycles rid the surface of any surface contaminants like carbon or oxygen, as can be observed in the survey spectrum (Figure S6) after the preparation. Ag 3d, Ag 3p and the fermi edge spectra were collected for each photon energy used in this study (Figure S7). The data was calibrated in each case to the centre point of the fermi edge (determined by differentiation of the fermi edge; blue dashed line in figure). There is no non-linearity observed in the data, indicating that any shifts in the data of this study is as a result of true chemical effects rather than instrumental artefacts.

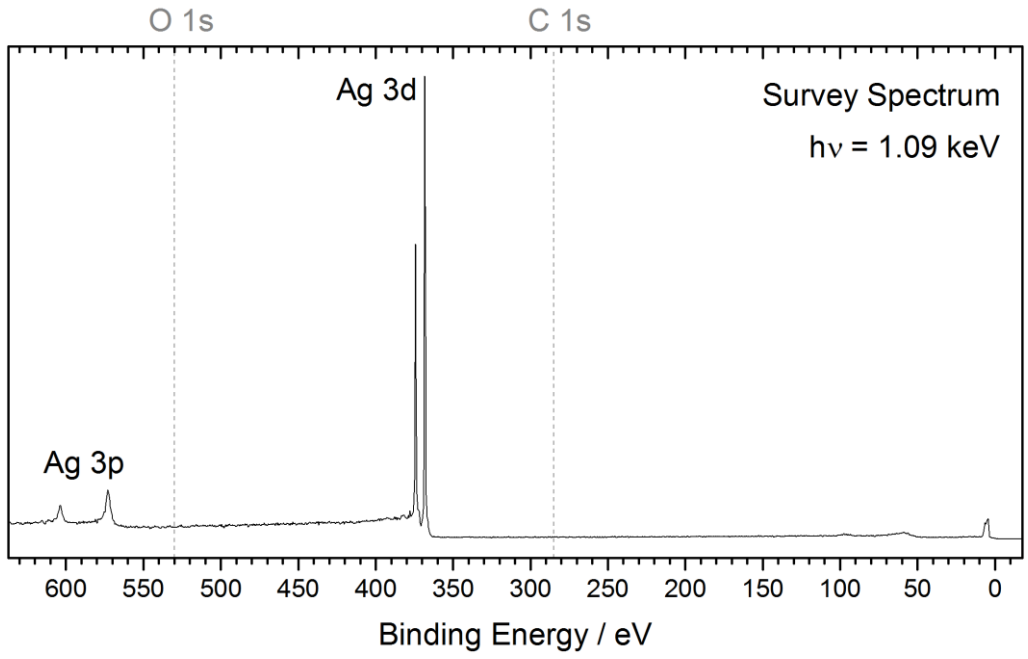

Figure S6. Survey spectrum of a Ag(111) single crystal after sputter-anneal preparation cycles. Dashed lines indicate the usual positions for O 1s and C 1s transitions.

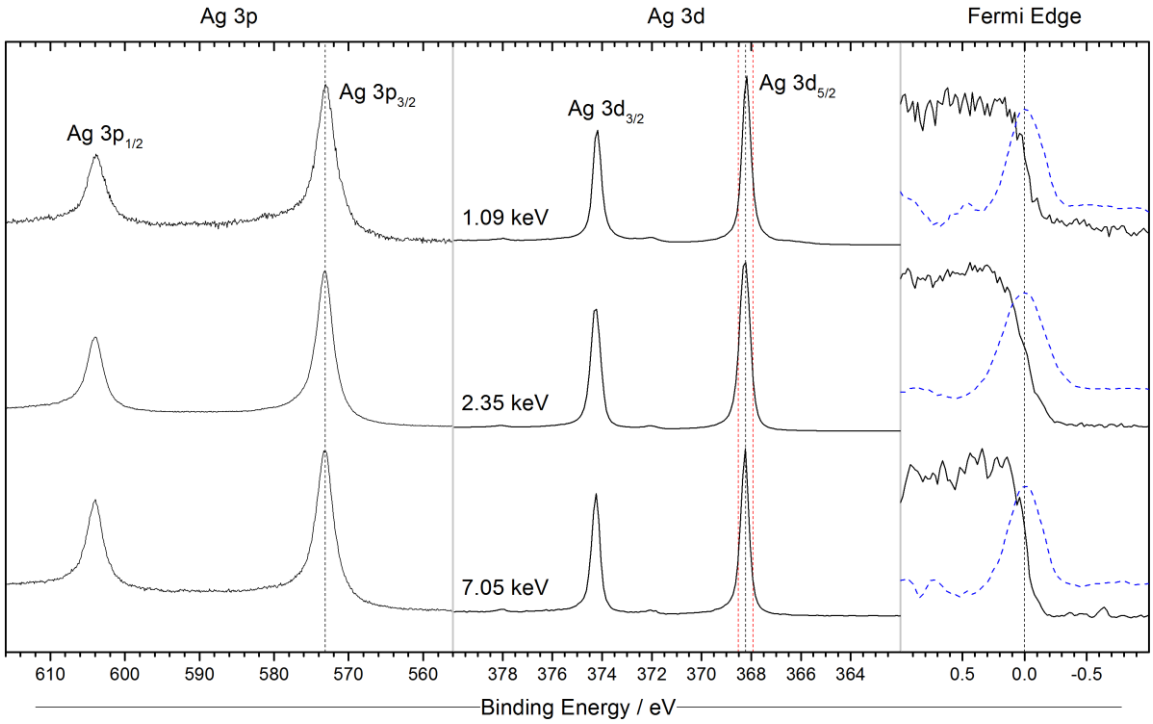

Figure S7. Energy-calibrated Ag 3p, Ag 3d and fermi edge spectra (differentials shown as dashed blue overlaid lines) of a Ag(111) single crystal after sputter-anneal preparation cycles. Red dashed lines around the Ag 3d(5/2) transition indicate ±0.3 eV from the peak position.

Note 5. Li 1s/Mn 3p spectra of $Li_{1.2}Ni_{0.2}Mn_{0.6}O_2$ samples.

The Li 1s/Mn 3p spectra measured with photon energies of 1.09 and 2.35 keV are presented in Figure S8.

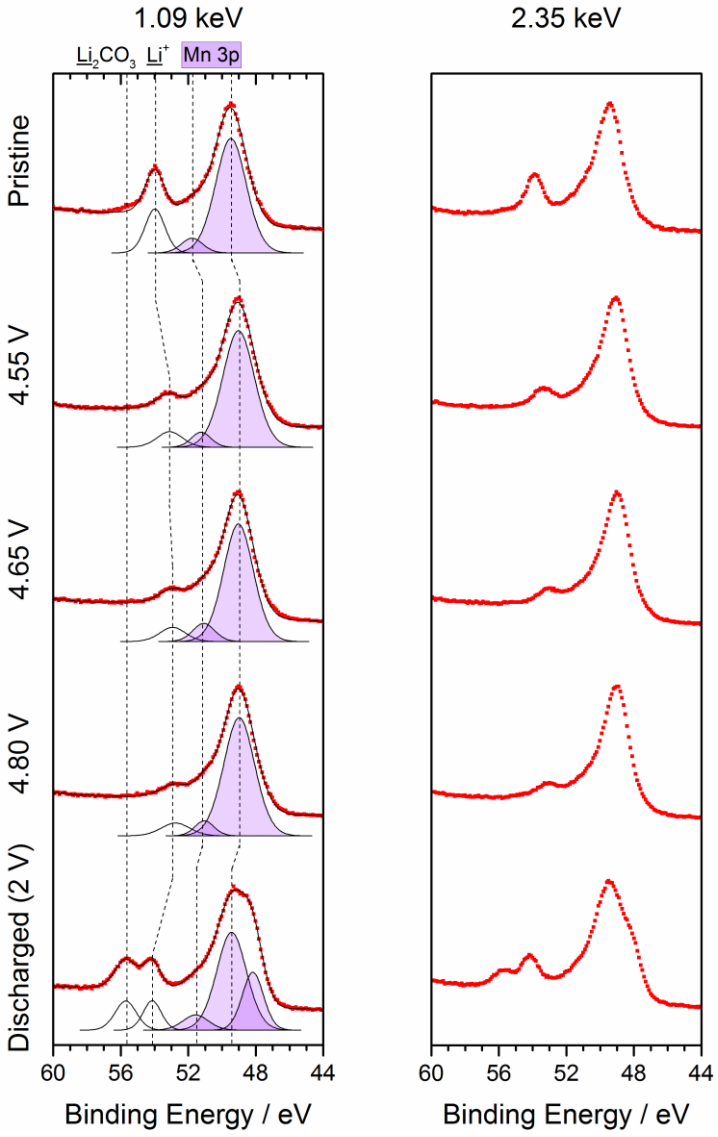

Figure S8. Li 1s and Mn 3p spectra for $Li_{1.2}Ni_{0.2}Mn_{0.6}O_2$ samples cycled to various points, measured using photon energies of 1.09 and 2.35 keV.

Note 6. Removal of the oxidised oxygen peak and subsequent fitting attempt.

Figure S9 shows the curved-fitted O 1s spectra for the layered material after removal of the oxidised oxygen (O^{n-}) peak. This demonstrates the requirement to include the peak in the fitting model and how a much larger area is filled by the O^{n-} peak for the surface spectra than the bulk spectra. Figure S10 demonstrates an attempt at fitting the model used in this study without the O^{n-} peak present, resulting in a very poor fit to the experimental data.

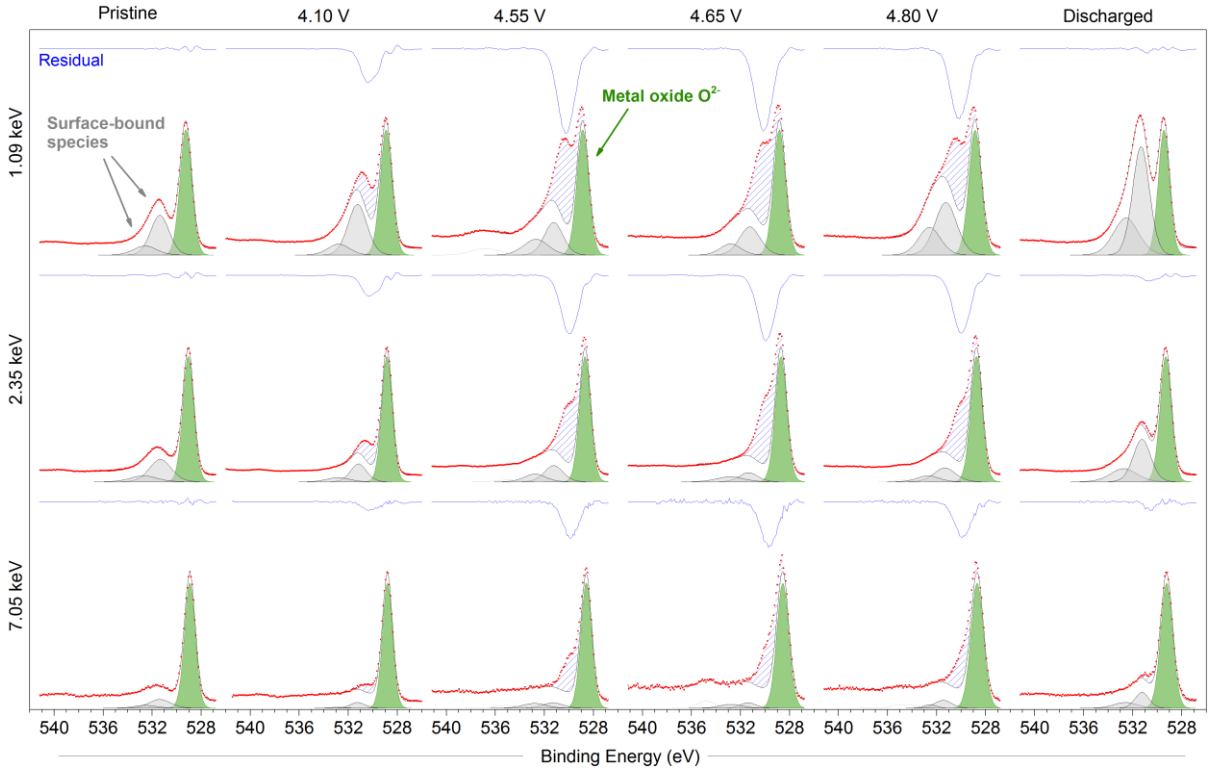

Figure S9. O 1s photoelectron spectra measured using three photon energies for $Li_{1.2}Ni_{0.2}Mn_{0.6}O_2$ at various states of charge. The O^{n-} peak has been removed post-fitting, to demonstrate the requirement for this peak to be included in the fitting model. Residual plots are show as a blue line above each spectrum. The blue hashed areas on each spectrum indicates the area under the data curve that is unfilled after removal of the O^{n-} peak.

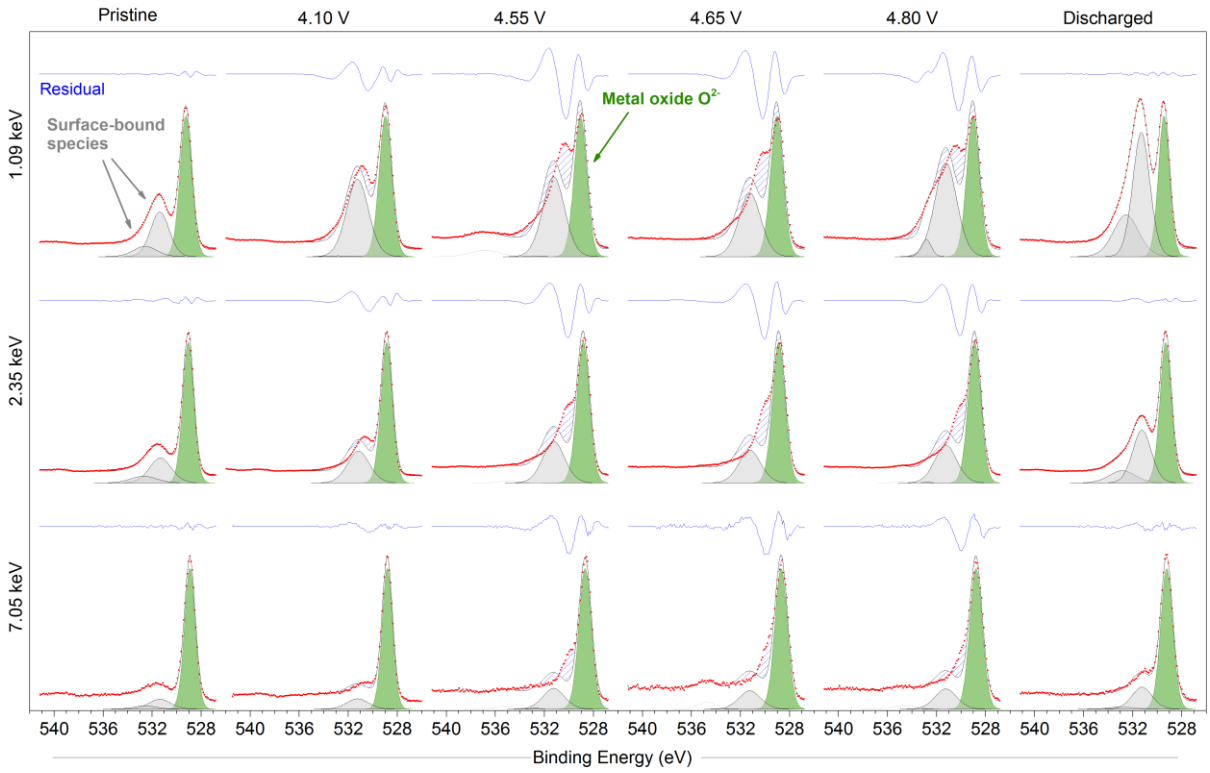

Figure S10. O 1s photoelectron spectra measured using three photon energies for $Li_{1.2}Ni_{0.2}Mn_{0.6}O_2$ at various states of charge. A fitting is attempted after removal of the O^{n-} peak, demonstrating that three peaks is not sufficient to fit such spectra. Residual plots are show as a blue line above each spectrum. The blue hashed areas on each spectrum indicates difference between the total curve fit and the spectrum data curve.

Note 7. Shifting of surface-bound species peaks on fixing of O^{n-} contribution.

In this study, we observe little evidence of newly formed surface species forming on the electrodes, as a result of electrolyte decomposition or a similar process. For example, the carbon black in the C 1s spectra remains by far the dominant species, without any suggestion for the formation of hydrocarbon, alkoxy, or carbonate containing species at the surface. We therefore fix the peak positions of the existing surface-bound species originating from the pristine material in the O 1s spectra. With these constraints in place, we then observe the depth dependant appearance and evolution of the O^{n-} peak. Figure S11 demonstrates an alternative approach, assuming that the oxidised oxygen concentration is uniform throughout the particle at 4.8 V and comprises 33 % of the total transition metal oxide contribution ($O^{n-}/[O^{n-} + O^{2-}]$ = 33 %). The result is that the oxidised oxygen peak is much less intense for the two lower depths and more intense for the greatest depth, than determined in the present study. In order to create a model that better fits the raw data, the peaks for the surface-bound species must be allowed to shift to lower binding energies by ~0.4 eV for the two lower photon energies, unrepresentative of what has been observed for other samples in this series. Even with this allowed shift, a poorer quality fit is obtained as indicated by the residual standard deviation. We determine that there is no chemical justification for allowing these peaks to shift as such, especially considering that a negative energy shift is representative of reduction processes, while the electrode should be in a highly oxidised state at 4.8 V. A depth dependency of the oxygen redox reaction, rather than a uniform profile throughout the particle, is thought to be the preferred model to properly explain the experimental data.

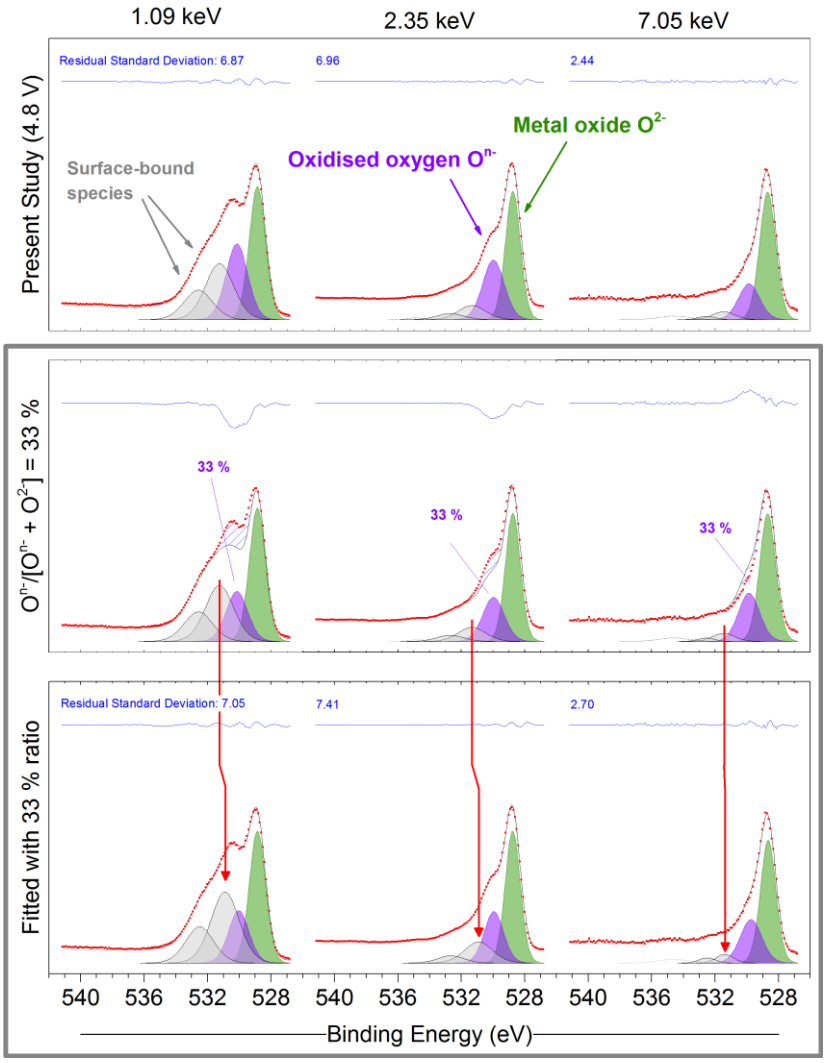

Figure S11. O 1s photoelectron spectra measured using three photon energies for $Li_{1.2}Ni_{0.2}Mn_{0.6}O_2$ at 4.8 V charge. The first row shows fitted data from the present study, the second row presents the data when the area of the O^{n-} peak is adjusted to make up 33 % of the total transition metal oxide contribution, while the third row demonstrates how the peaks for surface-bound species must shift unjustifiably to fill/relieve the intensity lost/gained by the adjustment.

Note 8. Spinel-phase $LiNi_{0.5}Mn_{1.5}O_4$ spectra.

As a material that does not exhibit oxygen redox activity,[10,11] the high-voltage spinel phase $LiNi_{0.5}Mn_{1.5}O_4$ makes for a good comparison to the Li-rich layered material. Cells with the spinel phase cathode were charged to 4.75 V and 5 V (Figure S12). We investigated the oxygen electronic states in the spinel material by measuring O 1s spectra (main text, Figure 3) for the pristine material and charged electrodes, at the three excitation energies 1.09, 2.35, and 7.05 keV. The fitting of a peak for O^{2-} and peaks for the surface species to the pristine spectra shows that there is a greater signal from the surface species relative to the oxide at all photon energies in this material, suggesting a thicker layer of surface-bound species than for the layered oxide.

For the fitting of the spectra, binding energies of the surface-bound species peaks remain constant, while the oxide peak is allowed to shift to lower BE on charge, as in the layered material during delithiation or oxidation of the transition metal. It is clear that no peak associated with an oxidised form of the oxide (O^{n-}) could be fitted in any of the spectra, for the surface or bulk measurements. Considering that such an intense signal is observed for a new oxidised oxygen species in the charged layered material, the absence of a similar indicator here is strong evidence that the high-voltage spinel-phase does not undergo an oxygen redox reaction and that the oxide structure is stable up to 5 V.

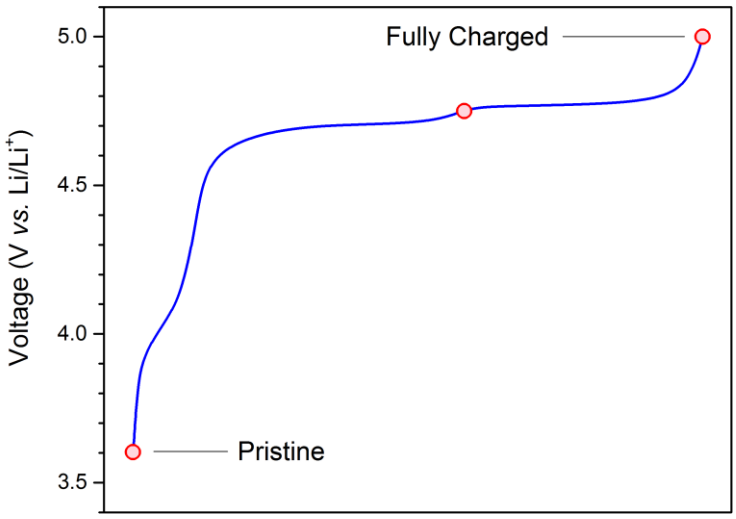

Figure S12. Voltage profile for cells with $LiNi_{0.5}Mn_{1.5}O_4$ electrodes, charged to 4.75, and 5 V *vs.* Li/Li^+. Red-coloured markers represent points at which samples were prepared for photoelectron spectroscopy measurements.

Note 9. Galvanostatic cycling curves for cells tested over multiple cycles.

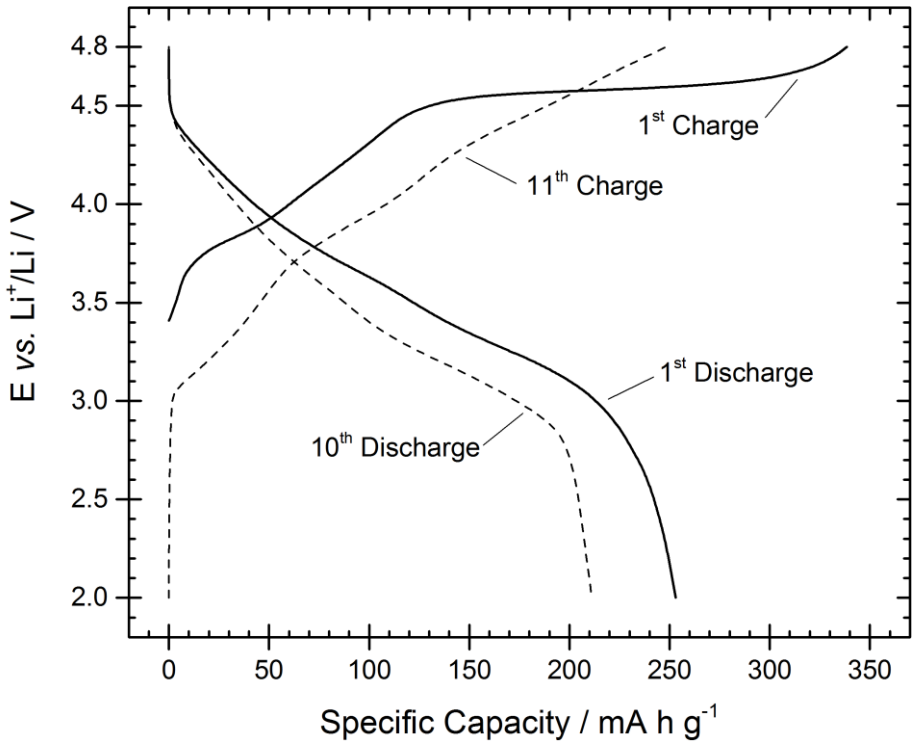

Figure S13. Galvanostatic cycling curves of $Li_{1.2}Ni_{0.2}Mn_{0.6}O_2$ *vs.* Li metal cells for the 1st cycle, 10th charge and 11th charge.

Note 10. Supplementary information related to the simulations and calculations.

Bulk structures:

The structure of the layered Li-excess material was simulated with the following composition: $Li_{1.17}Ni_{0.25}Mn_{0.58}O_2$. Following the footsteps of previous publications on the same material[12], several starting geometries were considered for the pristine structure and supercells containing 24 formula unit (Li28Ni6Mn14O48, 96 atoms in total) were created from each. The cation ordering within the transition metal layers was generated using the Python Materials Genomics tool (pymatgen)[13]. The most stable structure was determined by first ranking the cation arrangements by their Ewald energies and then by their DFT energies calculated with GGA+U (U equals 3.9 eV for Mn[14] and 6 eV for Ni[15]). The most stable arrangements were fully optimised with HSE06.

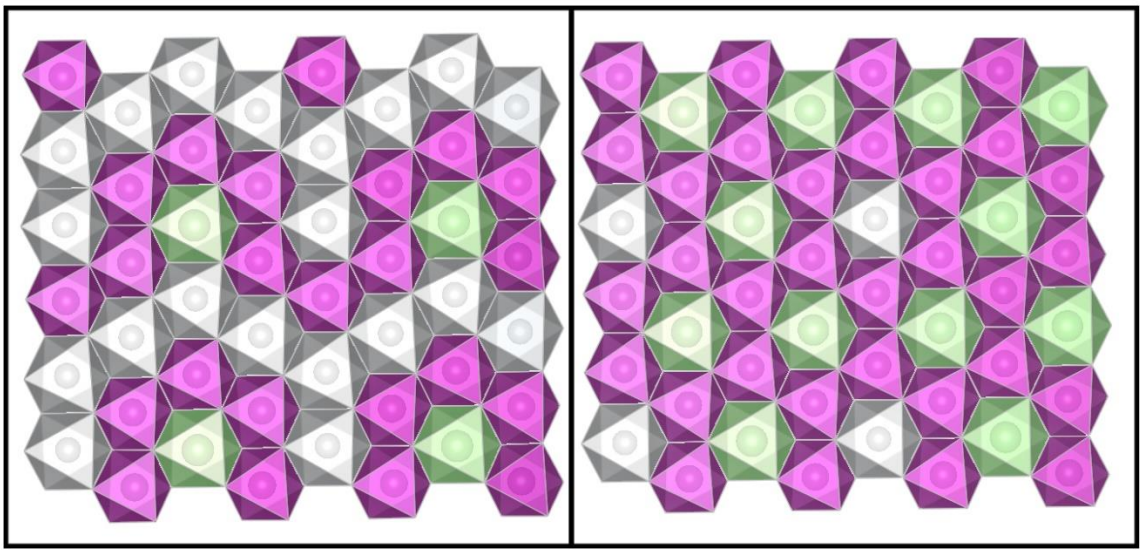

Figure S14. Cation ordering in the transition metal layers: The applied unit cell (based on the 2x1x2 supercell of Li_2MnO_3) contains two transition metal layers, which have slightly different cation ordering but in a similar arrangement as it was described by Xu *et al.*.[16] The lithium ion is coordinated to 5 Mn and 1Ni in one layer, while it is surrounded with 6 Mn in a honeycomb arrangement in the other. (Mn = purple, Li=green, Ni=grey)

It was experimentally detected that the Li is rather surrounded by another type of ions than form clusters in the transition metal layer[16,17], and the cation arrangement in Figure S14 is consistent with previous computational studies on this material.

After modelling the pristine structure, we continued to optimise several different Li^+ arrangements for the delithitated phases by using the same enumeration technique as described above to generate structures of $Li_{1.17-x}Ni_{0.25}Mn_{0.58}O_2$ (x=0.0, 0.5, 0.67, 0.83 and 1.0).

XPS calculations:

The core level binding energies (E_{CL}) of the O 1s electrons were evaluated with the initial state approximation[18–23] in which the energy to remove an electron from a certain core orbital is assumed to be equal to the negative difference between the Kohn-Sham eigenvalue of the investigated core state (ε_{KS}) and the Fermi level (ε_F):

$$-E_{CL} = \varepsilon_{KS} - \varepsilon_F \qquad \text{eq. 1}$$

We note that, within the framework of PAW potentials, the obtained core level energies are not directly comparable with experimentally obtained absolute values, neither with the initial state nor the more sophisticated final state approximation. Furthermore, with the application of a hybrid functional, in which the core states and valence states are treated differently in the nonlocal HF exchange,[24] the absolute values of core level energies are completely meaningless. Nevertheless, the application of hybrid functional is essential not just for the accurate prediction of the band gap but for the prediction of transition metal[25] and oxygen redox activity[26,27] during the charging process.

Considering only the core level shifts (the differences between binding energies), spin-polarised DFT calculations applying PAW and GGA+U for the O 1s core electrons were shown to be generally reliable in the past, even with the initial state approximation (since the frozen core only contains the 1s electrons).[19] Consequently, provided an adequate reference material exists, the obtained absolute

binding energy values with the DFT can be shifted with a reference based correction term into the environmentally observed energy region.

To ensure that the HSE06 and GGA+U calculations result in the same oxygen core level shifts when there is no alteration between the predicted oxidation states, we compared the average eigenvalues of the O 1s core states ($\bar{\varepsilon}_{O1s}^{HSE}$, and $\bar{\varepsilon}_{O1s}^{GGAU}$) for the pristine material and the chosen reference system: Li_2MnO_3 in Table S2. In both cases, we found a constant core level energy difference ($\bar{\varepsilon}_{O1s}^{HSE-GGAU}$ is -436.9 eV) between the two functionals, regardless of the environment of the oxygen. However, if we calculate the mean value of the O 1s core states for structures with partial Li content (x=0.67 and 0.5), we see a larger deviation in the energy, which is clearly relatated to the description of oxygen redox. While applying the HSE06 functional predicts oxygen oxidation within the structure and therefore results in ~1.4 eV difference in eigenvalues, the GGA+U results do not contain oxidised oxygens. Based on this observation, we assumed that HSE06 values can also be shifted with respect to a reference material.

Table S2. Average O 1s eigenvalues are calculated by HSE ($\bar{\varepsilon}_{O1s}^{HSE}$) or GGA+U ($\bar{\varepsilon}_{O1s}^{GGAU}$) and their difference ($\bar{\varepsilon}_{O1s}^{HSE-GGAU}$) for structures with x=1.17, 0.67 and 0.5 Li content and for Li_2MnO_3. In case of partially delithitated structures the core state eigenvalues of the supposed O^{2-} and O^- species were separated and their difference were calculated too. (All values are in eV.)

x	O type	$\bar{\varepsilon}_{O1s}^{HSE}$	$\Delta\bar{\varepsilon}_{O^{2-}/O^-}^{HSE}$	$\bar{\varepsilon}_{O1s}^{GGAU}$	$\Delta\bar{\varepsilon}_{O^{2-}/O^-}^{GGAU}$	$\bar{\varepsilon}_{O1s}^{HSE-GGAU}$	$\Delta\bar{\varepsilon}_{O^{2-}/O^-}^{HSE-GGAU}$
Li_2MnO_3	**O^{2-}**	-64.8 (0.0)	-	-501.8 (0.0)	-	-436.9 (0.00)	-
1.17	**O^{2-}**	-64.8 (0.3)	-	-501.7 (0.4)	-	-436.9 (0.03)	-
0.67	**O^{2-}**	-66.3 (0.5)	1.5	-503.0 (0.5)	0.1	-436.7 (0.1)	1.4
	O^-	-67.8 (0.0)		-503.1 (0.2)		-435.2 (0.2)	
0.5	**O^{2-}**	-66.7 (0.6)	1.4	-503.7 (0.5)	0.0	-437.0 (0.2)	1.4
	O^-	-68.1 (0.4)		-503.7 (0.2)		-435.6 (0.3)	

In the pristine $Li_{1.17}Ni_{0.25}Mn_{0.58}O_2$ material every oxygen atom is directly coordinated to six metal ions (Li^+, Mn^{4+} or Ni^{2+}) in an octahedral coordination but the exact environment can differ in the type of

the coordinating cations. Most of the oxygen atoms are coordinated to 4 Li^+ and 2 Mn^{4+} (4Li/2Mn, 46%), however, there are also oxygens surrounded by 3 Li^+, 2 Mn^{4+} and 1 Ni^{2+} (3Li/2Mn/1Ni, 29%) or 3 Li^+, 1 Mn^{4+} and 2 Ni^{2+} (3Li/1Mn/2Ni, 21%), while a few anions have 4 Li^+, 1 Mn^{4+} and 1Ni^{2+} (4Li/1Mn/1Ni, 4%) coordinated to them. By differentiating between the O 1s core level binding energies depending on the direct coordination environment, we can single out the binding energies of 4Li/2Mn oxygens and use the following equation (eq 2) to shift their calculated core level energies into the right energy region:

$$E_{corr}^{4Li/2Mn} = E_{exp}^{Li_2MnO_3} + (E_{calc}^{4Li/2Mn} - \langle E_{calc}^{Li_2MnO_3} \rangle) \qquad \text{eq. 2}$$

Where $E_{exp}^{Li_2MnO_3}$ is 529.4 eV, the experimentally measured binding energy of the O 1s electrons in the Li_2MnO_3 crystal,[28] in which every oxygen atom is in the 4Li/2Mn coordination. $\langle E_{calc}^{Li_2MnO_3} \rangle$ is the average binding energy calculated for this material using eq.1 and the same computational details used for $Li_{1.17}Mn_{0.58}Ni_{0.17}O_2$ (66.4 eV) and $E_{calc}^{4Li/2Mn}$ is the binding energy of one oxygen in the Li-rich oxide.

The binding energies of every other O 1s electrons in the pristine material are adjusted relative to the corrected values of 4Li/2Mn oxygens. The spectra of the partially delithiated structures are shifted considering the relative change in the core level energies of every oxygen compared to the corrected values of the fully lithiated structure.

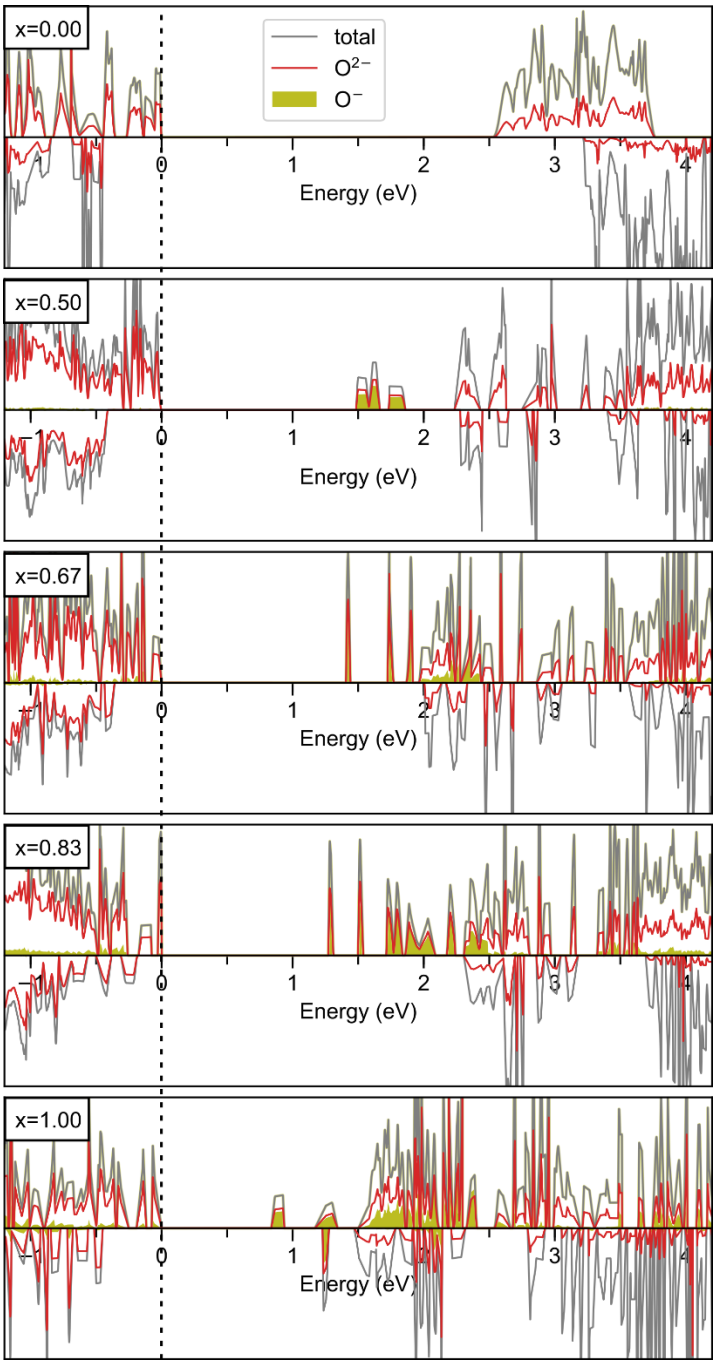

Figure S15. Total and partial density of states (DOS) plot for the $Li_{1.17-x}Ni_{0.25}Mn_{0.58}O_2$ structure with varying Li content (x=0.0, 0.5, 0.67, 0.83 and 1.0). The Fermi level is set to 0 eV. Plotting the pDOS for only the oxygen ions with magnetic moment close to -0.8 μ_B (filled yellow plot) demonstrates that the lowest unoccupied states are mostly related to these species. The fully delithitated structure (x=1.0) is an exception, in which the lowest unoccupied states are related to the oxidised Ni ions as well as the oxygens.

Note 11. STEM images of $Li_{1.2}Ni_{0.2}Mn_{0.6}O_2$ samples.

STEM images show a disordered rocksalt phase formed at the surface in the charged LiRich LMNO material. Lithium layers are filled with transition metal atoms in the disordered rocksalt layer.

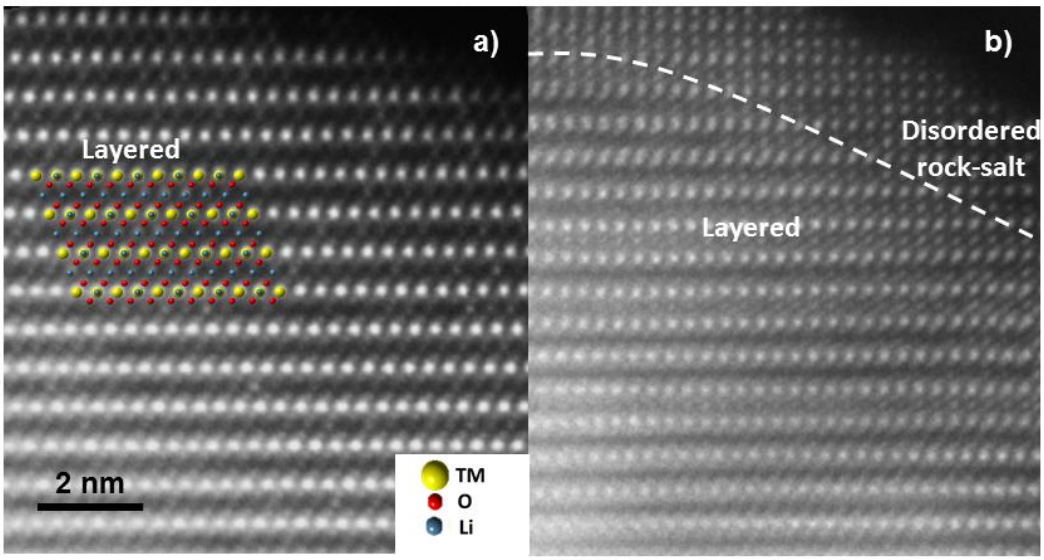

Figure S16. High resolution ADF-STEM images of a) pristine and b) charged (4.5V) layered LMNO.

References

1 A.B. Christie, in *Methods of Surface Analysis: Techniques and Applications*, ed. J. M. Walls, Cambridge University Press, 1989, p. 342.

2 S. Tanuma, C. J. Powell and D. R. Penn, *Surf. Interface Anal.*, 1994, **21**, 165–176.

3 M. P. Seah and W. A. Dench, *Surf. Interface Anal.*, 1979, **1**, 2–11.

4 K. Shimoda, T. Minato, K. Nakanishi, H. Komatsu, T. Matsunaga, H. Tanida, H. Arai, Y. Ukyo, Y. Uchimoto and Z. Ogumi, *J. Mater. Chem. A*, 2016, **4**, 5909–5916.

5 D. Foix, M. Sathiya, E. McCalla, J.-M. Tarascon and D. Gonbeau, *J. Phys. Chem. C*, 2016, **120**, 862–874.

6 M. Sathiya, G. Rousse, K. Ramesha, C. P. Laisa, H. Vezin, M. T. Sougrati, M.-L. Doublet, D. Foix, D. Gonbeau, W. Walker, a S. Prakash, M. Ben Hassine, L. Dupont and J.-M. Tarascon, *Nat. Mater.*, 2013, **12**, 827–835.

7 G. Assat, D. Foix, C. Delacourt, A. Iadecola, R. Dedryvère and J.-M. Tarascon, *Nat. Commun.*, 2017, **8**, 2219.

8 B. Philippe, M. Hahlin, K. Edstro m, T. Gustafsson, H. Siegbahn and H. Rensmo, *J. Electrochem. Soc.*, 2015, **163**, A178–A191.

9 R. Azmi, V. Trouillet, M. Strafela, S. Ulrich, H. Ehrenberg and M. Bruns, *Surf. Interface Anal.*, 2018, **50**, 43–51.

10 G. Gabrielli, M. Marinaro, M. Mancini, P. Axmann and M. Wohlfahrt-Mehrens, *J. Power Sources*, 2017, **351**, 35–44.

11 M. A. Kebede, S. N. Yannopoulos, L. Sygellou and K. I. Ozoemena, *J. Electrochem. Soc.*, 2017, **164**, A3259–A3265.

12 D.-H. Seo, J. Lee, A. Urban, R. Malik, S. Kang and G. Ceder, *Nat. Chem.*, 2016, **8**, 692–697.

13 S. P. Ong, W. D. Richards, A. Jain, G. Hautier, M. Kocher, S. Cholia, D. Gunter, V. L. Chevrier, K. A. Persson and G. Ceder, *Comput. Mater. Sci.*, 2013, **68**, 314–319.

14 H. Kim, D. J. Kim, D. H. Seo, M. S. Yeom, K. Kang, D. K. Kim and Y. Jung, *Chem. Mater.*, 2012, **24**, 1205–1211.

15 H. Chen, G. Hautier, A. Jain, C. Moore, B. Kang, R. Doe, L. Wu, Y. Zhu, Y. Tang and G. Ceder, *Chem. Mater.*, 2012, **24**, 2009–2016.

16 B. Xu, C. R. Fell, M. Chi and Y. S. Meng, *Energy Environ. Sci.*, 2011, **4**, 2223.

17 J. Bréger, M. Jiang, N. Dupré, Y. S. Meng, Y. Shao-Horn, G. Ceder and C. P. Grey, *J. Solid State Chem.*, 2005, **178**, 2575–2585.

18 S. Lizzit, A. Baraldi, A. Groso, K. Reuter, M. V. Ganduglia-Pirovano, C. Stampfl, M. Scheffler, M. Stichler, C. Keller, W. Wurth and D. Menzel, *Phys. Rev. B*, 2001, **63**, 205419.

19 L. Köhler and G. Kresse, *Phys. Rev. B*, 2004, **70**, 165405.

20 É. Guille, G. Vallverdu and I. Baraille, *J. Chem. Phys.*, , DOI:10.1063/1.4904720.

21 É. Guille, G. Vallverdu, Y. Tison, D. Bégué and I. Baraille, *J. Phys. Chem. C*, 2015, **119**, 23379–23387.

22 P. B. Paramonov, S. A. Paniagua, P. J. Hotchkiss, S. C. Jones, N. R. Armstrong, S. R. Marder and J. L. Bredas, *Chem. Mater.*, 2008, **20**, 5131–5133.

23 N. Pueyo Bellafont, F. Vines, W. Hieringer and F. Illas, *J. Comput. Chem.*, 2017, **38**, 518–522.

24 M. Schlipf, RWTH Aachen University, 2012.

25 V. L. Chevrier, S. P. Ong, R. Armiento, M. K. Y. Chan and G. Ceder, *Phys. Rev. B*, 2010, **82**, 075122.

26 D. H. Seo, A. Urban and G. Ceder, *Phys. Rev. B - Condens. Matter Mater. Phys.*, 2015, **92**, 1–11.

27 H. Chen and M. S. Islam, *Chem. Mater.*, 2016, **28**, 6656–6663.

28 S. Han, Y. Xia, Z. Wei, B. Qiu, L. Pan, Q. Gu, Z. Liu and Z. Guo, *J. Mater. Chem. A*, 2015, **3**, 11930–11939.